

TENSILE PROPERTIES ENHANCEMENT RESPONSE OF A413 AND A356 ALUMINUM CASTING ALLOYS TO DIRECT WATER SPRAY PROCESSING

Ali Kheirabi, S. M. A Boutorabi and Mehdi Divandari

School of Metallurgy and Materials Engineering, Iran University of Science and Technology, 16846-13114 Narmak, Tehran, Iran

Mohammad Pourgharibshahi 

Department of Chemical and Materials Engineering, Sirjan University of Technology, 78137-33385 Sirjan, Iran

Copyright © 2023 American Foundry Society
<https://doi.org/10.1007/s40962-023-01045-2>

Abstract

Direct water spraying (DWS) is an approach similar to ablation casting using direct impingement of water spray on the solidifying casting but is modified in that it no longer relies on eroding removal of the sand bound by water-soluble binders. A removable part of the sand mold is withdrawn during the process, and water is directly sprayed on the exposed casting surface. Two commercial casting Al alloys, i.e., A413 with short to zero and A356 with a wider freezing range, were processed by the DWS method. Comparison of the conventional and DWS-processed castings with respect to the microstructure and mechanical properties was evaluated via computer-aided thermal analysis, metallography, and tensile testing. The average ultimate tensile strength (UTS) increased from 126

to 193 MPa in A356 and 139–159 MPa in A413 by applying the DWS method. The elongation was increased from 2.8 to 11% in the DWS A356 and from 1.8 to 5% in the DWS A413. The secondary dendrite arm spacing (SDAS) was decreased from 80 μm in A356 to 44 μm and from 68 μm in A413 to 32 μm in the respective DWS-processed counterparts. The experimental results confirmed that a longer freezing range is more favorable with the DWS process, producing improved castings with higher tensile properties.

Keywords: aluminum alloy, water Spray, freezing range, thermal analysis, mechanical properties, simulation

Introduction

Despite significant advancement in production of defect-free casting products, further improving the as-cast mechanical properties of the Al–Si alloy casting parts is still challenging. The ablation casting process is a casting process innovated to promote the conventional sand-casting process by both making possible the application of higher heat extraction/cooling rates and enhancing the recyclability of the molding materials. The heat extraction rate depends on different parameters including casting modulus,¹ material and thickness of mold and coating,^{2,3} and the air-gap layer thickness.^{2,4} A higher cooling rate during alloys solidification can result in the refinement of microstructural features, including SDAS of the primary α -

Al phase, micro-porosities, and iron-bearing intermetallics.^{5–8} A sufficiently high cooling rate can affect the morphology and distribution of the intermetallics.^{9,10} It can promote the adjoining or coalescence of the primary phase dendrite arms earlier in the solidification range, thereby increasing the tensile properties either during the solidification or after complete solidification, and through this, it can enable producing hot-tear-free shape castings.¹¹ This, however, depends on a technique to accelerate the heat extraction from the melt or the solidifying casting to increase the cooling rate.¹²

In the ablation casting (AC) process, as soon as the mold cavity becomes filled, water is sprayed on the mold to dissolve the sand binder and washing it out for either preventing formation or eliminating the already formed air-gap layer between the casting and the mold walls, which can result in a more refined microstructure and higher

ultimate tensile strength and elongation when comparing to conventionally sand-cast counterparts.^{13–19} Despite no delaying time in the case of AC due to lack of information about the kinetics of binder dissolution, the delaying time to formation of cortex layer is highly important.

A major challenge faced by the foundries working with the original AC process has been the process sensitivity to type of the water-soluble binder in such a way that a minimal change in the chemical formulation may lead to significant repeatability problem with respect to the casting mechanical properties.²⁰ The coolant medium, the onset time of spraying, and duration are some of other key factors that depend on the binder formulation. Boutorabi and Taghipourian used the green sand (bentonite as the binder) instead of the proprietary water-soluble binder, and the results have been promising.^{15,18} A major challenge with using the green sand might be the uncontrolled washing of the mold which can result in uneven cooling and increasing the tearing risk of casting solid surface during mold demolishing stage. Direct water spraying (DWS), as a modified version of the original ablation process, has been developed to address these problems. The conventional Na_2SiO_3 binder activatable by CO_2 gas is used instead of the proprietary water-soluble binders.²⁰ This method releases the air gap by allowing the removal of a specific part of the mold just after the formation of an early solidified cortex around the casting. The removed part makes it possible the coolant media (here is water) being directly sprayed on the exposed surface of the solidifying casting which significantly promotes the heat extraction rate.²¹

Study on the intense-cooling processes to further clarify the effect of different dependent and independent variables is advancing. The enhancement response of all alloys to cooling rate is not the same. In the present study, two well-known commercial Al-Si alloys, that is A413 and A356, with relatively short (10 °C) and longer (40 °C) freezing ranges, respectively, were cast via conventional sand casting and by the DWS technique to investigate how different would be the enhancement in tensile properties of the alloys by the intense cooling rate. The solidification behavior, cortex layer formation time, microstructural features, porosity defects, and the as-cast mechanical properties are discussed.

Experimental Procedure

The flowchart of the work in the current study is shown in Figure 1. The different stages will be explained in detail in the current section. Throughout the paper, DWS stands for the direct water spraying process, and CSC is a short form for referring to conventional sand casting. During the DWS process, the mold cap is removed from the cope to let the

water directly sprayed on free surface of the solidifying casting.²⁰

Melts Preparation and Casting Procedure

The pattern geometry along with the gating and feeding systems is shown in Figure 2.^{18,19} The gating system ratio was 1:2:4 (sprue/runner/ingate) and designed in the bottom-pouring form to keep the melt flow unpressurized at a velocity below the critical velocity of aluminum alloys (0.5 m/s) to avoid turbulence and air entrapment during the mold filling.^{2,22,23} Inside the runner, a 40×60 mm filter was used just after the sprue to either decrease the melt velocity or filter out the inclusions.^{1,22–24} Because of the limited number of experiments with this geometry and to reduce the pattern-making costs as well as eliminating the need for parting line and cope/drag in the flask, the pattern was made of EPS (expanded polystyrene) to be vaporized during a preheating stage. After ramming the sand around the pattern and blowing it sufficiently using CO_2 gas, the EPS pattern was eliminated by a torch to provide the mold cavity in a single flask. No draft is required on the EPS pattern, and hence, the dimensional precision is relatively higher than the multiple-use patterns. It should be noted that this strategy in pattern-making is not integral of the DWS process and was kept in this paper only for the sake of convenience. The casting was side-gated from the riser.

The molding material, including that of the cap in the cope (in the model for DWS processing), was made of silica refractory granules with sodium silicate (Na_2SiO_3) as the binder to be activated by CO_2 gas.

Approximately, 8.5 kg of A356 was melted inside a coated cast-iron crucible and super-heated up to 730 °C. At this temperature, the melt was Ar-purged for 180 s for degassing²⁰ using a diffuser lance and the gas level was empirically assumed to be reduced sufficiently after the degassing process. No inoculant agent or protective flux was used. The molten alloys were poured with mass rate of 0.8 kg/s at 720 °C. The same procedure was carried out for preparing molten A413 alloy super-heated up to 700 °C and poured at 680 °C. Both molds were preheated up to 100 °C.²⁰ To have the Weibull analysis plot, all the process was repeated two times. The actual chemical composition of the alloys was determined using the spark emission spectroscopy (SES) and is presented in Table 1.

Casting Simulation

The *ProCast® V.2019* commercial software was used to validate the gating system efficiency and solid cortex thickness evaluation. The feeding and solidification behavior of the two alloy castings was analyzed using the *Solid Fraction Module* of the software. The alloys chemical

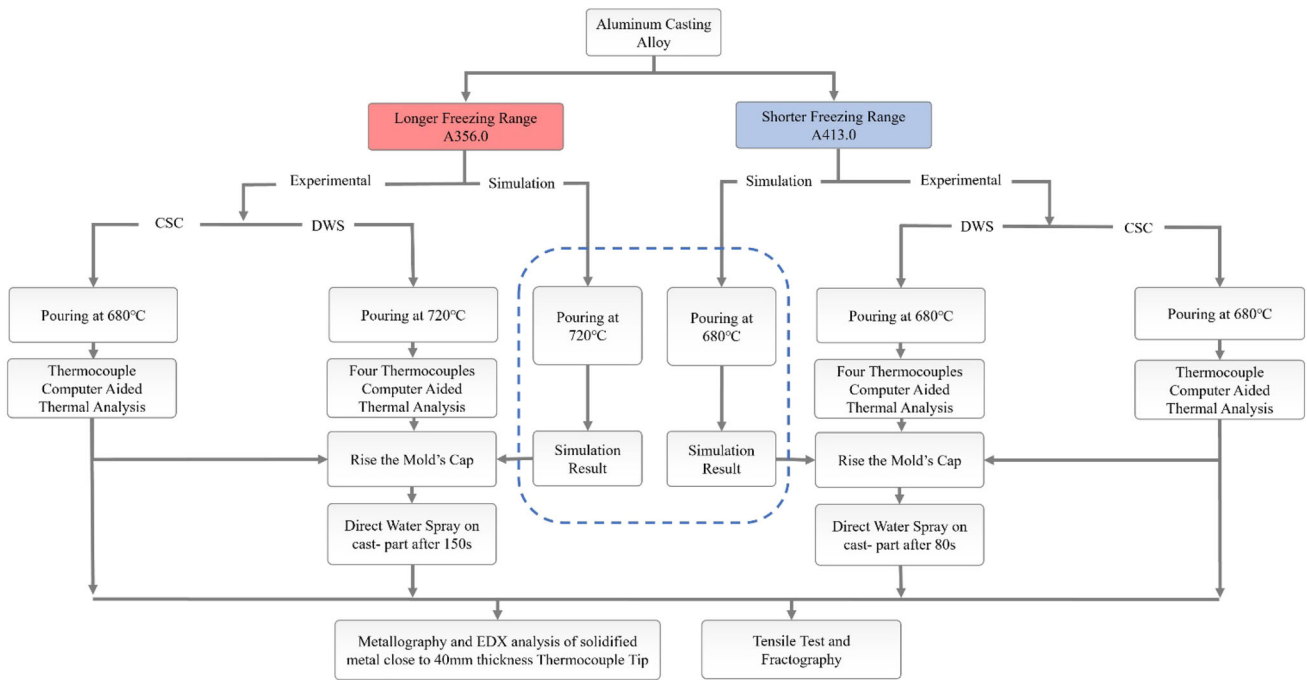


Figure 1. Flowchart of the experimental procedure.

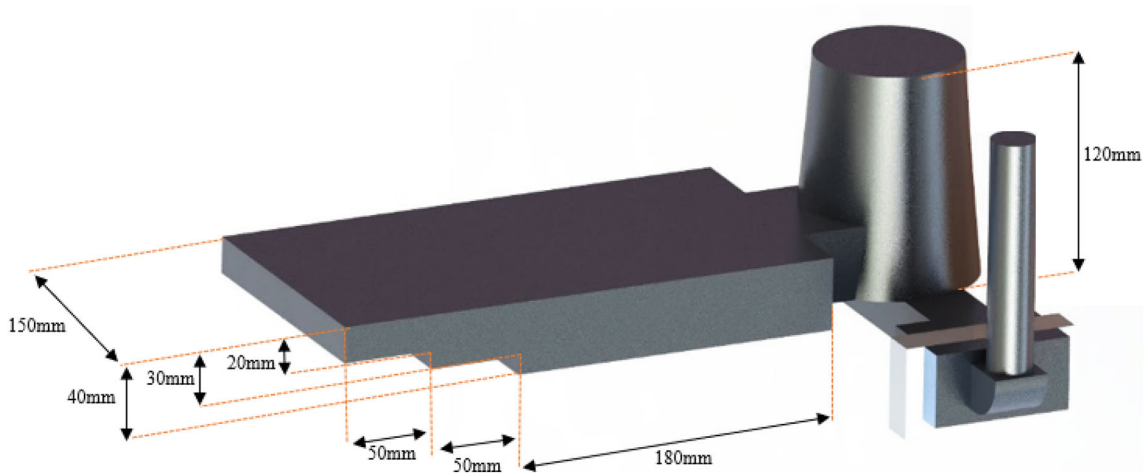


Figure 2. The geometry of the pattern showing the stepped casting along with the gating and feeding system.

Table 1. Chemical Composition (wt%) of Alloys Used in this Study and Its Standard Range

Alloy		Si	Mg	Fe	Cu	Mn	Al
A413	Sample	11	0.11	0.6	0.55	0.20	Bal.
	Standard	11.0–13.0	0.0–0.1	0.0–1.3	0.0–1.0	0.0–0.35	Bal.
A356	Sample	7.5	0.5	0.14	0.14	0.05	Bal.
	Standard	6.5–7.5	0.45–0.55	0.0–0.2	0.0–0.2	0.0–0.1	Bal.

composition was inputted according to Table 1. The back-diffusion was considered with the *Solid Diffusion Model* in the material database. There reveals no error in the gating

system (design, yield ratio, melt flow, feeding function). The feeding function was examined with Niyama module in the software. Figure 3 represents the *Interfacial Heat*

Transfer Coefficient (IHTC) of the two alloys in the sand mold. Other simulation parameters are presented in Table 2. It should be noted that currently no specific module exists to simulate ablation casting. The *Thermo-calc*® commercial software was used to predict the equilibrium phase diagram and solidification path of the two alloys (based on the alloys chemical composition in Table 1).

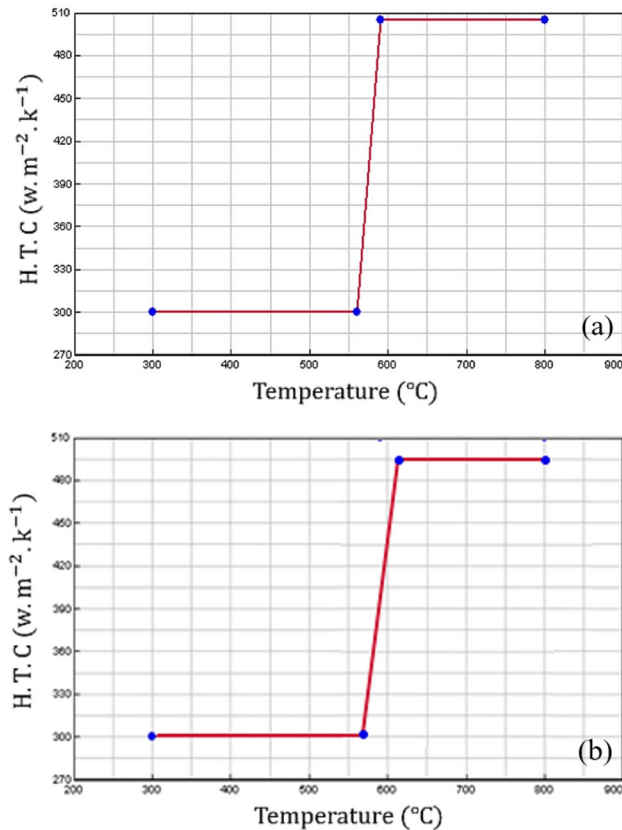


Figure 3. Heat transfer coefficient for (a) A413 and (b) A356 alloys in sand casting mold.

DWS Casting

Different stages of the DWS process are the same as those described by Kheirabi et al. [20] which is schematically shown in Figure 4.

Stages (a, b) in Figure 4 are exactly what occurs during conventional sand casting (CSC). At stage (c), at a given time (precisely calculated based on CSC simulation and thermal analysis of the alloys castings) at which an exterior solid layer (Cortex) of sufficient thickness covers the solidifying casting, the tightly closed cap is disassembled and removed and spraying commences. The proper time of cap withdrawal and spraying relies on the CSC cooling curve and solidification rate. The first is based on the fact that the best response by the conventional ablation process is achieved when water is sprayed while the primary α -Al phase is at the growth stage (in the solidification range before the onset of eutectic temperature).¹⁸ The second is important because the cortex is formed at the surface and supports the casting to prevent geometrical and dimensional changes by the spraying pressure. This time is 150s after mold filling for A356 and 70s for A413. Removal of the cap eliminates the air gap; thereby, the water directly touches the exposed surface of the casting. Hence, the IHTC is to be increased at stage (d). Care was taken to protect the feeder from being sprayed. Some macro-image related to the steps during the DWS processing is shown in Figure 5. The water flow rate was 0.7 L/s.

Thermal Analysis

The computer-aided thermal analysis (CATA) method was used to track the solidification path of the alloy. To record the cooling curve of the alloys in the casting condition, a K-type thermocouple connected to an acquisition setup and a personal computer is embedded at the center of the 40

Table 2. Initial and Boundary Conditions for Sand-Casting Simulation

CSC casting process parameters.	Values	
	A413	A356
Alloy	A413	A356
Pouring temperature (°C)	680	720
Filling time (s)	8	8
Interfacial heat transfer coefficient (IHTC) between casting and sand mold (W/m ² K)	As shown in Figure 3	
Liquidus temperature (°C)	585	615
Ambient temperature (°C)	30	30
Cast total meshes – mesh size (mm)	2000000 – 1	2000000 – 1
Mold (silica sand) temperature (°C)	100	100
Mold (silica sand) total meshes – mesh size (mm)	1000000 – 2	1000000 – 2

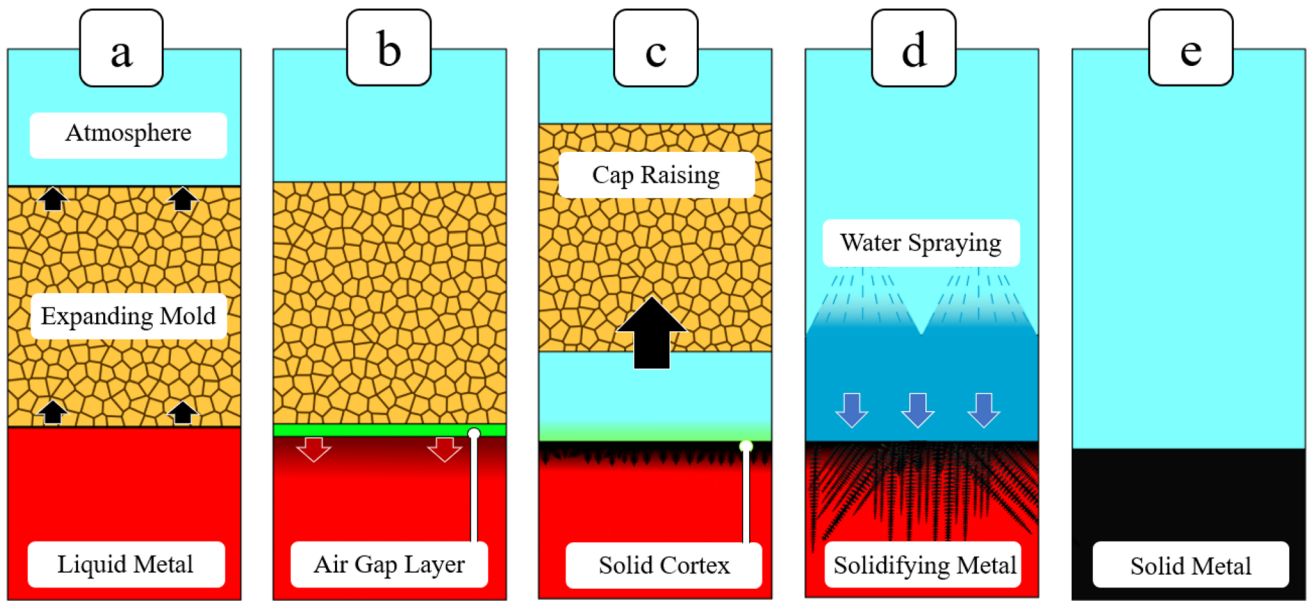


Figure 4. The schematic representation of different stages of the DWS Ablation Casting process (adapted from²⁰).



Figure 5. DWS processing steps, (a) cap assembly and venting, (b) pouring, (c) cap withdrawal and spraying, and (d) mold collapsing and removing the casting.

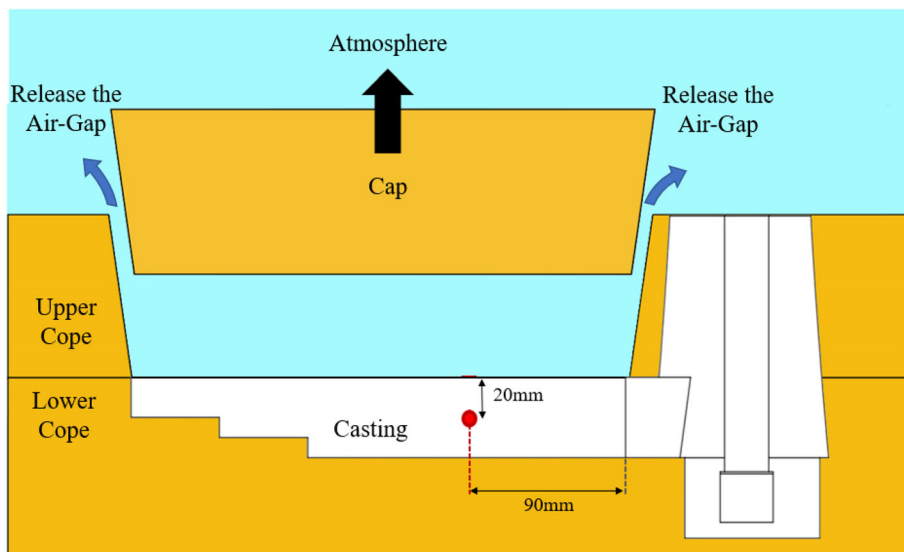


Figure 6. Schematic of the designed mold with raised cap for DWS processing. The thermocouple location is shown in the mold cavity (adapted from²⁰).

mm thickness step of the casting, as shown in Figure 6. The thermal data acquisition frequency was 1 data/s and monitored online on the personal computer. The related

temperature-time ($T-t$) graphs and the associated first derivations were calculated and plotted for a more precise thermal analysis.

Characterizations

Structure Examinations

The samples for metallography purposes were cut from the 40 mm thickness steps at the closest location to the tip of the thermocouple to make it possible correlating the thermal events with the observed phases in the microstructure. Grinded and polished samples were etched by HF solution and studied by optical microscopy and ImageJ image processing software for secondary dendrite arm spacing (SDAS) and inter-lamellar eutectic spacing (ILES) measurement. The linear intercept method is used to measure the SDAS and the ILES.²⁵ The metallography samples and fractured surface of the tensile test specimens were studied by field emission gun scanning electron microscopy (FEG-SEM). The energy-dispersive spectrometry (EDS) point scans was used three times per each feature to determine chemical composition of the revealed phases.

Tensile Testing

Nine tensile testing specimens were extracted from the casting. Five of them belong to the 40 mm step, respecting the feeding direction, two from 30 mm and two from 20 mm. The circular specimens were machined in small size according to the ASTM E8/E8M-16a to 9 mm diameter and 36 mm gauge length. Tensile testing was carried out with an Instron 1195-5500r machine at a 1 mm/min cross-head speed.

Results and Discussion

Simulation Results

The vertical slice cutoff views of the 40 mm thickness steps in A356 and A413 are presented in Figure 7, illustrating the thickness of the cortex layer in this zone. According to the

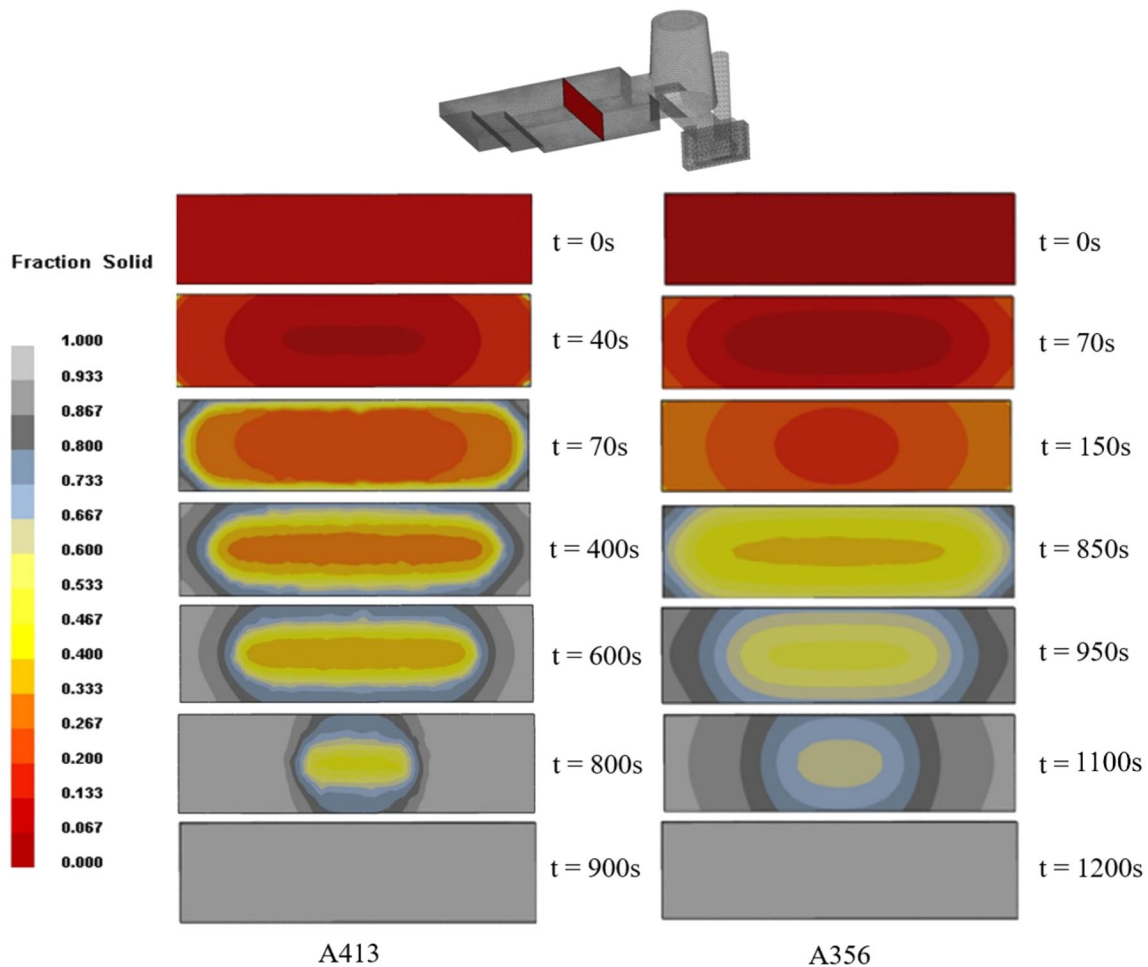


Figure 7. Solid fraction map at the mid-section of the 40 mm step, resulting from CSC casting simulation.

simulation results, with a 70s lag after complete filling, the cortex solid layer forms on the surface of A413 casting. The casting bulk remains at a low f_s (solid fraction) surrounded by a thin covering solid layer. For A356 casting, the cortex layer forms at around 150 s after complete filling because of the longer freezing range. Because of the relatively wider solidification range of A356, the cortex layer

is thicker and took more time to cover the casting surface than in A413.

The ablated surfaces of the DWS castings at 9 s after solidification start are shown in Figure 8 as compared to those of the CSC castings. There were rough bumps on the surface of the DWS castings with less than 2 mm height due to the interaction of the sub-cortex molten metal with

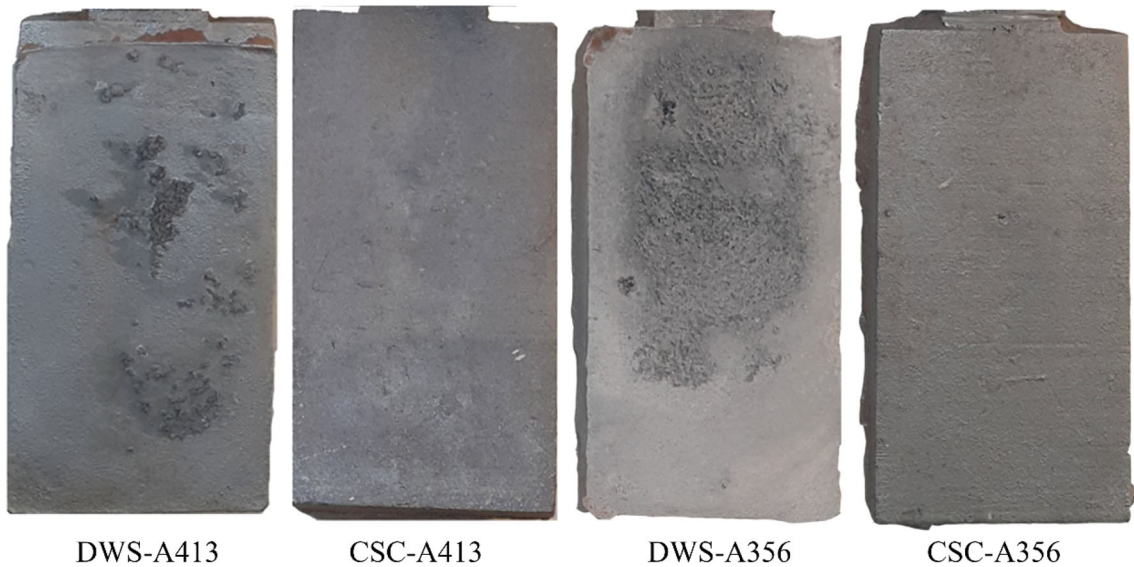


Figure 8. The casting top surfaces in as-cast condition.

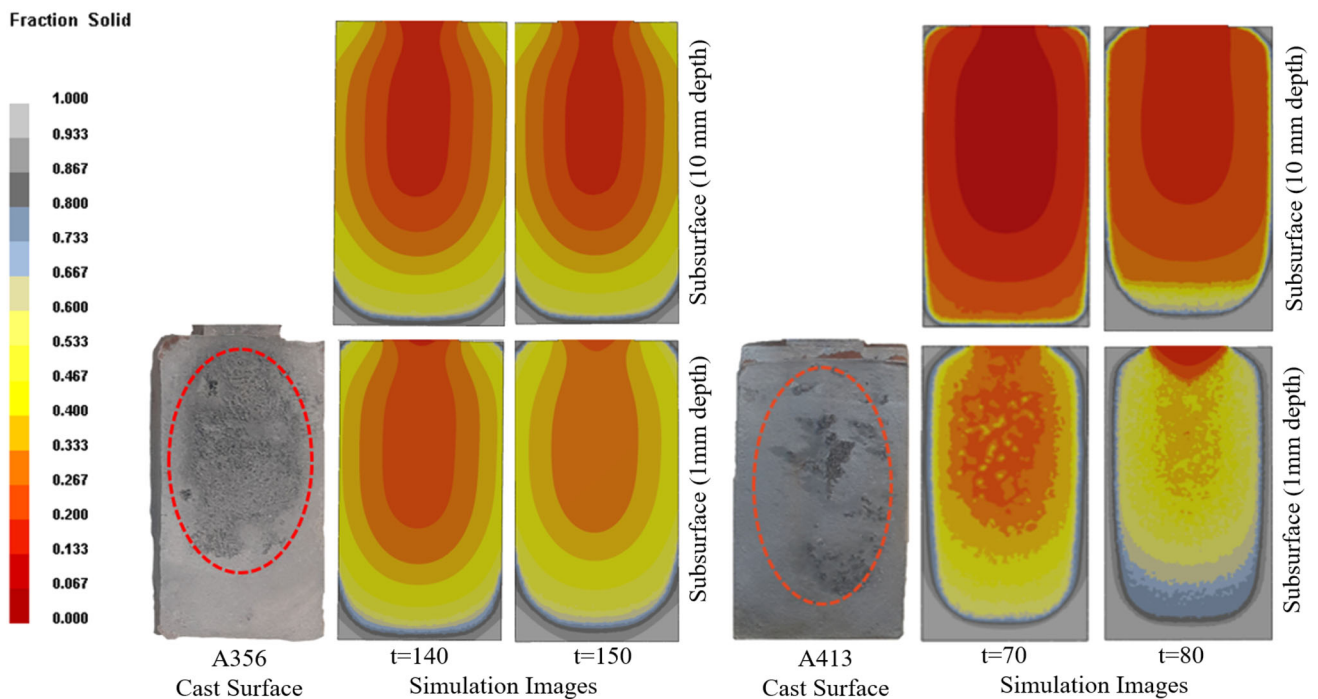


Figure 9. As-cast surface of the DWS-A356 and DWS-A413 casting beside the simulated images of the casting part, surface, and 10 mm under the surface within the CSC process and the at spraying time.

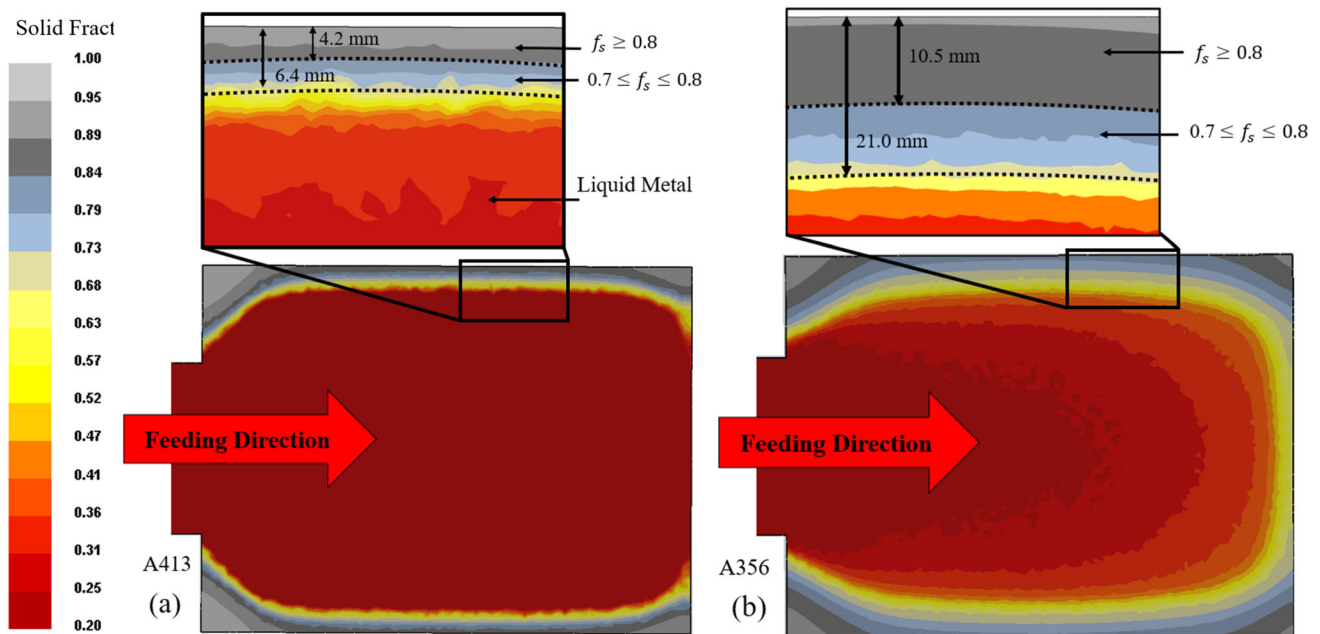


Figure 10. The thickness of the solid-fraction layers in the central plane: (a) skinny solidification of A413 vs (b) solidification over a wider freezing range in A356 alloys.

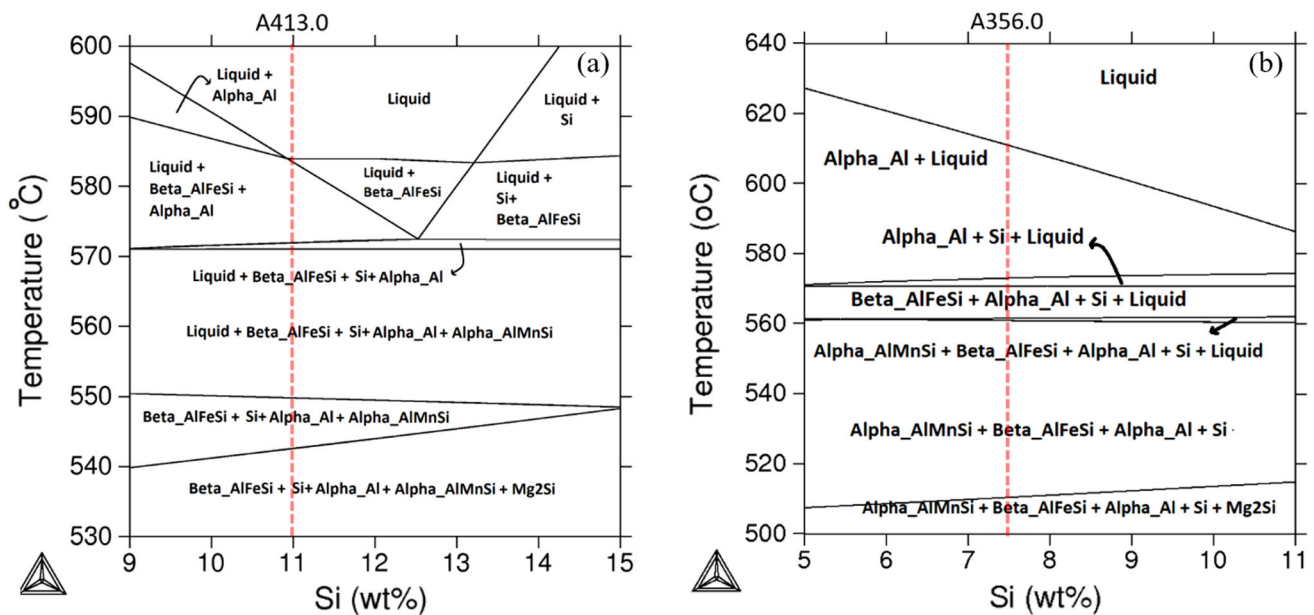


Figure 11. The calculated equilibrium isopleth phase diagram using the ThermoCalc® software related to the (a) A413 and (b) A356 alloys.

the water droplets. Simulation results presented in Figure 9 show the solid fraction regions at spraying time in both surface and the center plane of the 40 mm steps. In the A356 castings, the bumps are of a smaller height compared to A413. According to Figure 8, simulation results can precisely predict the bumps on the surface of the casting in the two DWS-processed alloys. In DWS A356, the map of the solidifying pattern (f_s) related to the surface and center

planes at 140s and 150s (close to cortex formation time) was not changed significantly because of the relatively wider solidification range of the alloy (Figures 7 and 9) and the progressively increasing viscosity. But at the same planes of the solidification maps in A413 during cortex formation time (70 s–80 s) a big difference is observed. The f_s value is increased at the central plane due to the relatively narrower isothermal zone during the

solidification. The sub-surface liquid reacts with the impacting droplets and resulted in a bump of higher amplitudes on the surface.

The location and thickness of the regions in the simulated situation according to their f_s contours are presented in Figure 10. At 70 s, in A413, the region with more than 0.8 f_s is of 4.2 mm thickness, and the thickness of the sublayer having $0.7 < f_s < 0.8$ is 2 mm. For A356 at 150 s, the cortex reaches at 10.5 mm thickness of f_s higher than 0.8 (cortex) and the thickness of the sub-cortex layer having $0.7 < f_s < 0.8$ is 10.5 mm.

For accurate interpretation of the cooling curves and the thermal analysis, the calculated isopleth phase diagram using the Thermocalc® software can be seen in Figure 11a and b. The alloys A413 and A356 are shown on the corresponding isopleth based on the chemical composition reported in Table 1.

According to Figure 11, the liquid phase can be persistent till the 550 and 560 °C for A413 and A356 alloys, respectively. Hence, the solidification range of the A413 alloy is rather larger, that is, 35 °C due to the Mn content of the alloy and the low melting point α -AlMnSi phase formed. Neglecting this low melting phase, solidification ends at 573 °C, and therefore, the solidification range of A413 alloy can be considered as short as 12 °C. Due to the negligible amount of Mn in the chemical composition of the A356 alloy, the solidification range of the alloy (50 °C) is not significantly affected by neglecting the α -AlMnSi phase. The solidification range of A356 alloy is, however, can be considered shorter by 10 °C by neglecting the β -AlFeSi phase due to the low Fe content of the alloy. Another interesting point in the isopleth diagram of A413 alloy is a critical silicon content beyond which the formation of β -AlFeSi precedes formation of α -Al phase. This critical value is calculated around 11wt% Si. The Si content of the A413 alloy in the present study is marginally higher than this value, and hence, it can be anticipated that the solidification of the alloy can be commenced by the formation of β -AlFeSi. This phase is atomically faceted and expected to be an efficient nucleation substrate for nucleation of the non-faceted α -Al phase, while the vice versa is not necessarily true according to the non-reciprocal theory.²⁶ Based on the phase diagram, by increasing the Si content above the critical value the formation temperature of α -Al is reduced meaning that the β -AlFeSi phase can grow and this can hinder efficient feeding causing significant shrinkage porosity defects. In the case of A356 alloy, β -AlFeSi phase is formed at a temperature much lower than that of the α -Al, and hence, no grain refinement of this type can be anticipated.

As far as the ablation processing of the two alloys are considered, the high rate of heat extraction and cooling rate may increase the nucleation rate of the β -AlFeSi particles

in the liquid A413 and thereby increasing the nucleation rate of the α -Al phase. At the same time, the increased segregation at the high cooling rate of the process and the fact that α -Al is not an efficient nucleant for the α -AlMnSi postpones the solidification end of the alloy to lower temperatures. This, however, can be beneficial to the mechanical properties of the alloy as the α -AlMnSi forms finer at a higher undercooling considering the ablation processing of the A356 alloy, with the high cooling rate no β -AlFeSi induced grain refinement can be anticipated. It is, however, possible postponing the formation of β -AlFeSi to lower temperature at which it can grow finer. It should be noted that the β -AlFeSi phase is a faceted phase, and hence, its nucleation on the α -Al phase requires a relatively higher undercooling. Thus, it can be deduced that ablation processing can promote formation of finer β -AlFeSi particles as they have to grow at a lower temperature.

Thermal Analysis

A356 Alloy

The A356 cooling curves and the corresponding first derivative related to the CSC and DWS processes are shown in Figure 12a and b, respectively. The typical microstructure of the alloy close to the thermocouple tip in CSC and DWS is shown in Figure 12c and d, respectively. The α -Al dendrites in the microstructure are observed below the corresponding cooling curve. In Figure 12c, the DAS is not recognizable in the CSC microstructure. However, in DWS (Figure 12d), the DAS, as well as dendrites spreading orientation, was clearly observable oriented along the solidification direction.

The equilibrium solidification can be assumed at the center of the 40 mm thickness; hence, the calculated phase diagram in Figure 11b can be used to interpret the peak revealed on the cooling rate curves in Figure 12a. The A356 alloy liquidus temperature is 610 °C. On the cooling curve, the label number (1) at 612 °C stands for the onset of solidification where the nucleation and growth of the primary α -Al phase commences; that is $L \rightarrow \alpha$ Al point (2) is for the primary α -Al dendrites grow into the liquid phase and progressively made it enriched in silicon and iron. A pre-eutectic interval occurs on the cooling curve that onsets at point (3) (around 584 °C) and ends when the eutectic starts to form at point (4), around 572 °C. This interval should not be misinterpreted as a peak related to phase formation.²⁶ This feature observes when the primary phase is not a suitable substrate for nucleation of the second phase.²⁷⁻³¹

Here, the surface of the α -Al dendrites is not an efficient substrate to catalyze the nucleation of the eutectic Si phase. Consequently, the solidification stops while the temperature reduces to provide further undercooling.²⁶ During the

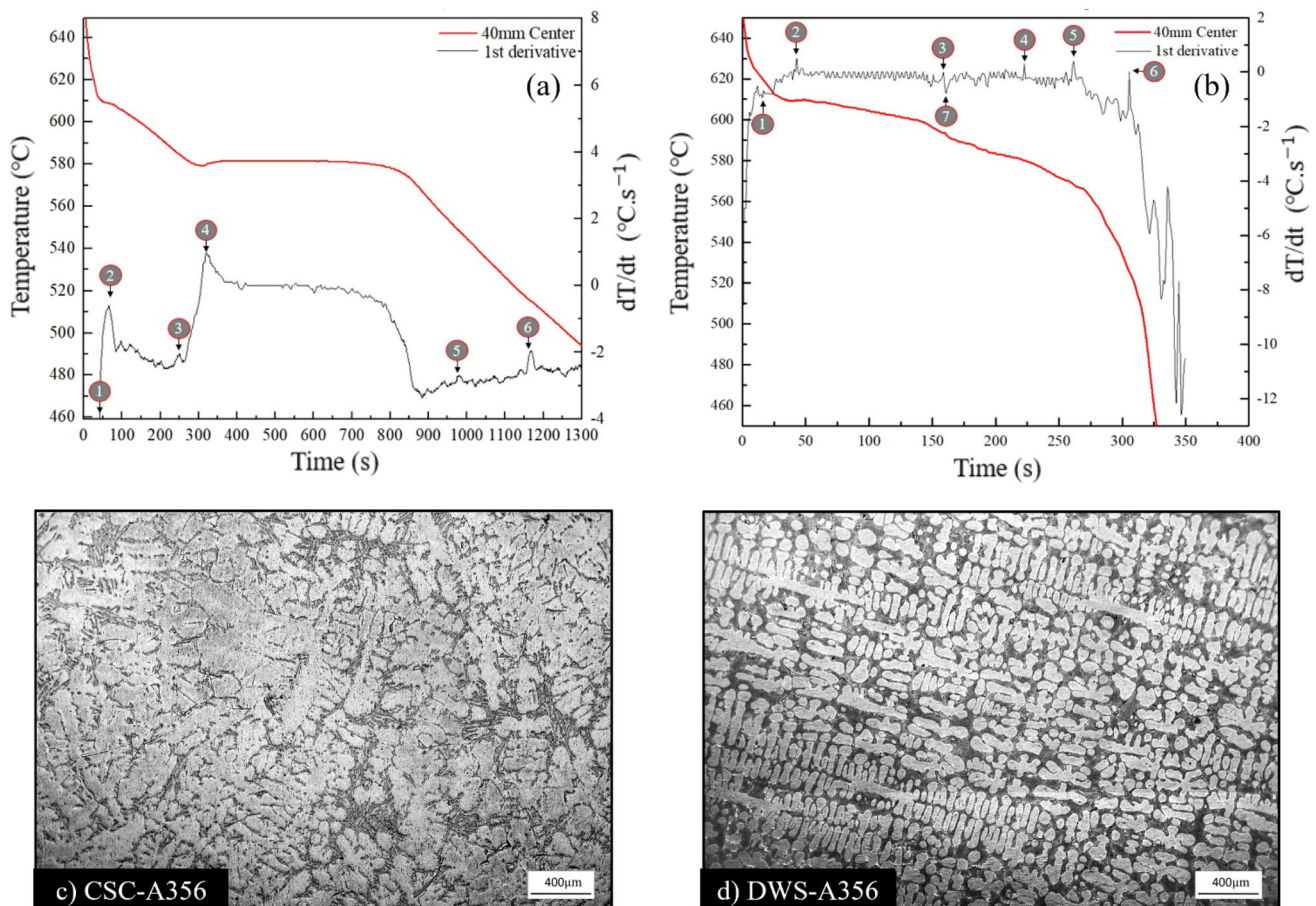


Figure 12. Thermal analysis and microstructure of A356 (a) cooling curve of CSC sample, (b) cooling curve of CSC sample of DWS process, (c) CSC coarse microstructure and (d) finer microstructure in AC.

solidification stop, the Si atoms are absorbed or back-diffused on the α -Al phase and finally nucleate Si via the adsorption heterogeneous nucleation.^{32,33}

After finishing the pre-eutectic interval by forming the eutectic Si at 572 °C, the surface of the Si particles can serve as highly efficient substrates for nucleation of the β -Fe phase. The peak related to the formation of the β -Fe phase is not discernible on the cooling rate curve. However, its appearance is evident in the microscopic images (as discussed later) as well as in the prediction of the isopleth phase diagram. The same is a trough for the eutectic transformation of the remaining liquid into the β -Fe and α -Fe phases, which is predicted by the isopleth diagram and EDS analysis. The solidification ends at around 560 °C (Point (5)). Point (6) is related to a solid-state reaction that is responsible for the formation of Mg₂Si. According to the location of the peak, Mg₂Si starts to form at around 512 °C, almost as predicted by the calculated phase diagram, i.e., 508 °C. The point (7) in Figure 12b is to show the starting point of water spraying on the casting.

Keeping in mind the possibility of the stoppage during solidification, a higher cooling rate at this stage could provide the required undercooling for non-stop growth of

the primary α -Al phase and thereby enhancing the mechanical properties of the alloy by letting it be interconnected with the eutectic α -Al. It should be noted that the nucleation of the Si phase as a result of the heterogeneous adsorption nucleation leads to the formation of a Si layer (lateral growth) on the primary α -Al phase surface which requires re-nucleation of the α -Al on it to allow the cooperative growth, which means the primary α -Al dendrite and eutectic α -Al is not interconnected.²⁶ Hence, according to the experimental thermal data in Figure 12a, a proper time for raising the cap and spraying would be before the onset of the pre-eutectic feature on the cooling curve, i.e., before point (2). Referring to the simulation results from Figures 7 and 9 illustrating that the cortex layer does not fully cover the casting before 150s, the best time interval for the water spraying is around 150s which is before the pre-eutectic interval (point (2)), labeled as number 7 on Figure 12b.

A comparison of the CSC microstructure in Figure 12c with that of the DWS shown in Figure 12d reveals that the DWS can decrease the SDAS size from 80 µm in CSC to 44 µm and the eutectic inter-layer distance from 20 µm in CSC to 2 µm.

A413 Alloy

Considering the isopleth phase diagram shown in Figure 11a, the solidification of the A413 alloy commences by forming the β -Fe intermetallic above the formation temperature of the primary α -Al phase (584 °C). Between the liquidus temperature and 572 °C, the stable phases are the liquid, β -AlFeSi, and primary α -Al. At 572 °C, the binary eutectic $L \rightarrow \alpha Al + Si$ takes place. From 571 to 550 °C, the remaining liquid is solidified as α -Fe. The Mg_2Si intermetallic compound is predicted in the phase diagram of the alloy to be formed at 543 °C, even though no Mg_2Si particles is observable in the related micrographs.

The cooling curves and the corresponding first derivative curves of the A413 alloy processed by CSC and DWS casting methods are shown in Figure 13a and b, respectively, along with the typical microstructure of the castings at the tip of the thermocouple after CSC (Figure 13c) and DWS processing (Figure 13d).

In Figure 13a, the point (1) refers to the liquidus temperature of the alloy at 582 °C where the primary α -Al phase starts to form, i.e., $L \rightarrow \alpha Al$. It should be noted that the

peak related to the formation of the β -Fe phase is not visible on the cooling rate curve due to the low Fe content of the alloy [33].

Similar to the A356 alloy, the pre-eutectic feature is revealed on the cooling rate curve of the alloy due to the low catalyzing effect of the primary α -Al phase as the nucleant for the eutectic Si phase. Point (2) refers to the stop of the solidification. Point (3) indicates the onset of the binary Al-Si eutectic reaction at 569 °C which is followed by the formation of the α -Fe phase, while the formation of the Si phase provides an efficient heterogeneous nucleation substrate for it. No peak on the curve could be related to the α -AlMnSi phase even though the EDS analysis evidenced its presence in the microstructure. Point (4) is the end of the solidification process (540 °C). The average DWS-SDAS is 32 μm , 47% finer than the CSC-SDAS (68 μm).²⁰

Mechanical Properties

The average results of the tensile tests on the CSC and the DWS specimens extracted from the 40 mm step are presented in Figure 14. The average ultimate tensile strength

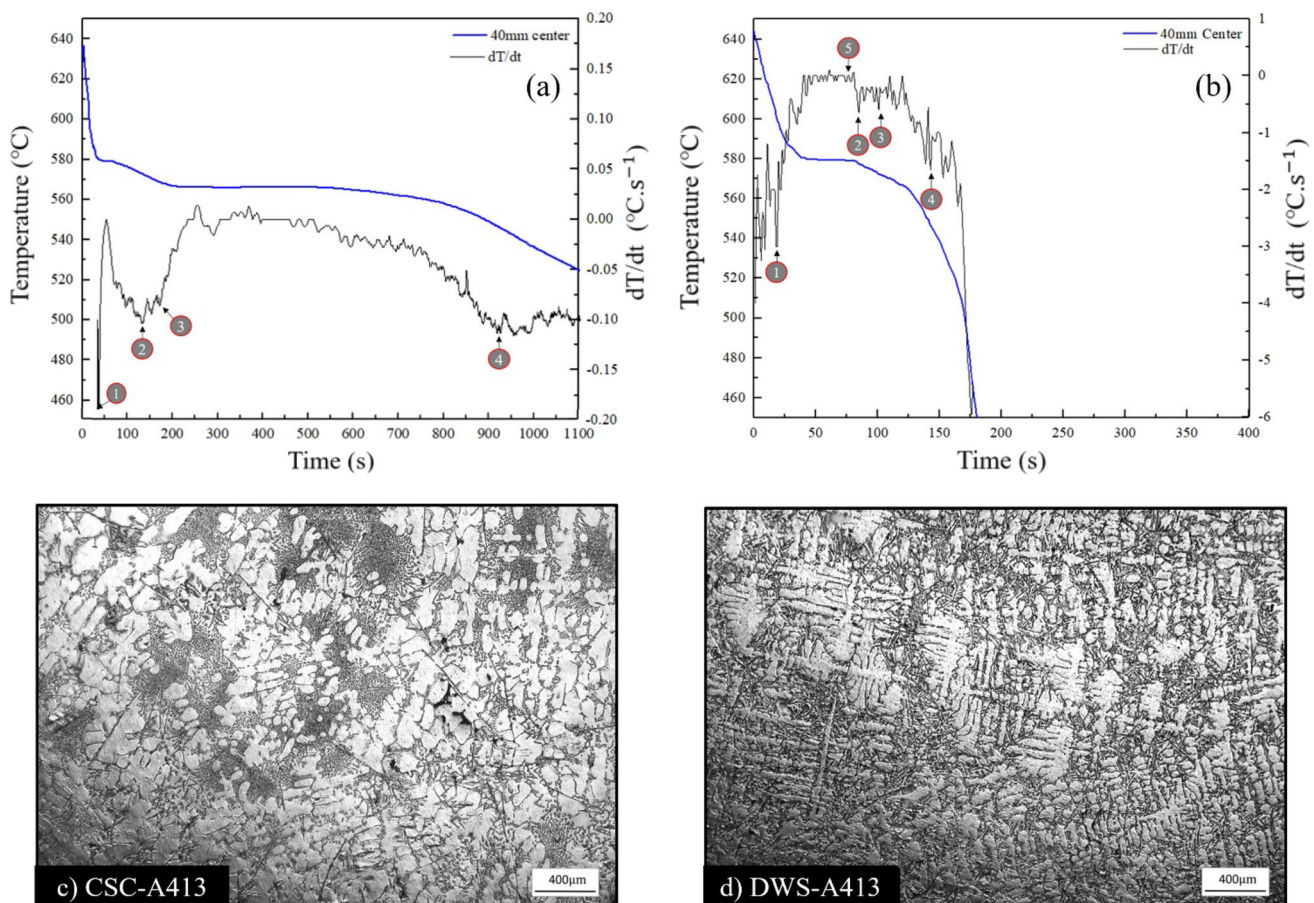


Figure 13. A413 Thermal analysis and microstructure. (a) Cooling curve that includes 1st derivative of CSC process. (b) Cooling curve that includes 1st derivative of DWS process, (c) coarse microstructure of the CSC process and (d) finer microstructure of the DWS-A413 sample.

(UTS) and elongation percentage (e_f) are enhanced with the DWS process. Figure 15 shows the distribution of UTS against e_f of all steps in the as-cast mode.

Distribution of the UTS by e_f in all steps of the casting part are plotted in Figure 15. According to Figures 14 and 15, the applied intense cooling rate during the DWS process increased the UTS and e_f of DWS samples in comparison with CS. It is due to the accepted fact that a higher cooling rate refines the microstructural features.^{20,34–39}

Figure 15 shows how the DWS process enhanced the tensile mechanical properties of the cast part and move the CSC results area to a higher value in both alloys.

The Weibull analysis of the UTS point for the 40 mm steps is plotted in Figure 16. All data belong to 40 mm steps. It shows that the distribution range of UTS for the DWS

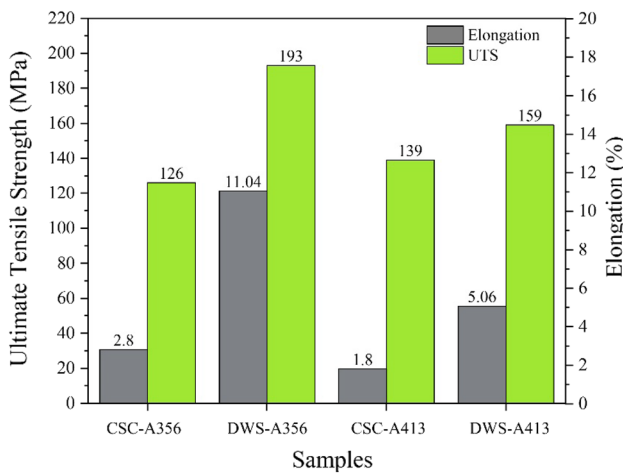


Figure 14. The UTS and e_f value for the as-cast samples produced by DWS and CS.

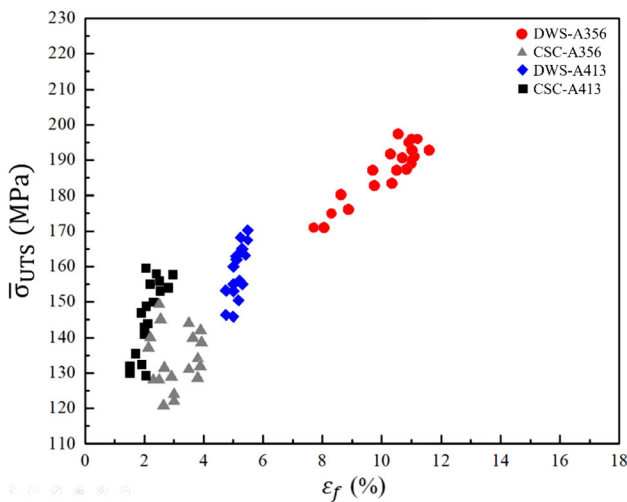


Figure 15. Distribution of UTS to e_f for all steps of the four casting types.

process provides a more reliable σ_{UTS} distribution compared to the CSC process.

The slopes of the fitted lines, the Weibull modulus, for DWS-A356, CSC-A356, DWS-A413, and CSC-A413 are 57.7, 29.9, 48.3, and 24.9, respectively. A356 shows a narrower tensile strength distribution in both castings compared to the A413 alloy. Therefore, it is expected to observe less variation in UTS tension in the cast part.

Figure 17 presents fractography SEM Images of tensile tests related to the A413 specimens. According to the EDS analysis, the CSC 413 sample experienced a brittle fracture on large Fe-bearing particles in the microstructure. Although evidence proved the presence of coarser micro-shrinkages in Figure 17b. This discontinuity reduces the bearing cross section in the tensile force, increasing the possibility of crack initiating location from its wall. The micro-shrinkage dimension in DWS A413 in Figure 17e size decreased because of the higher cooling rate. All other microstructural components decreased, such as SDAS, which is bigger in the CSC (Figure 17b) than the DWS (Figure 17e); then, the samples showed more resistance against the shear stress, and there was no cleavage fracture evidence.

Fractography of A356 samples investigated in Figure 18 by SEM images. The CSC-356 sample was broken at lower tension stress. Regarding the EDS analysis, the cleavage fracture evidence occurred on the Fe-bearing intermetallic particle in Figure 18c. The micro-shrinkage in the CSC-A356 structure is presented in Figure 18b, which was not traceable in the DWS-356 sample. Figure 18e exhibits the cup and cone mechanism signs on the fracture surface that indicates the ductile fracture of DWS-A356.

The ductile fracture of the DWS-A356 can evidence a higher degree of bridging by the neighboring dendrites.

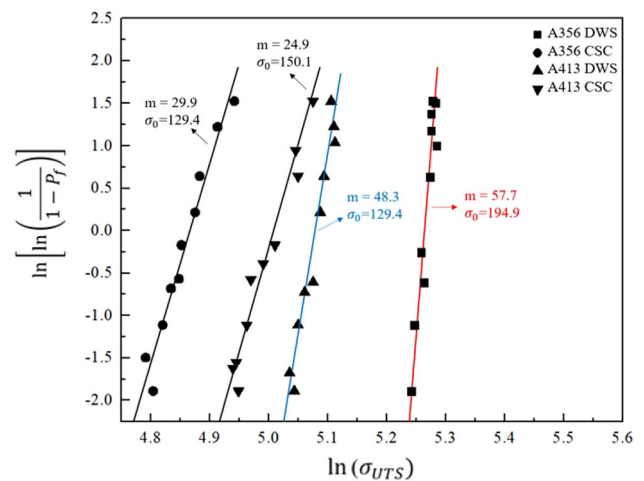


Figure 16. Weibull analysis Plotted for tensile test of 40 mm step of all samples.

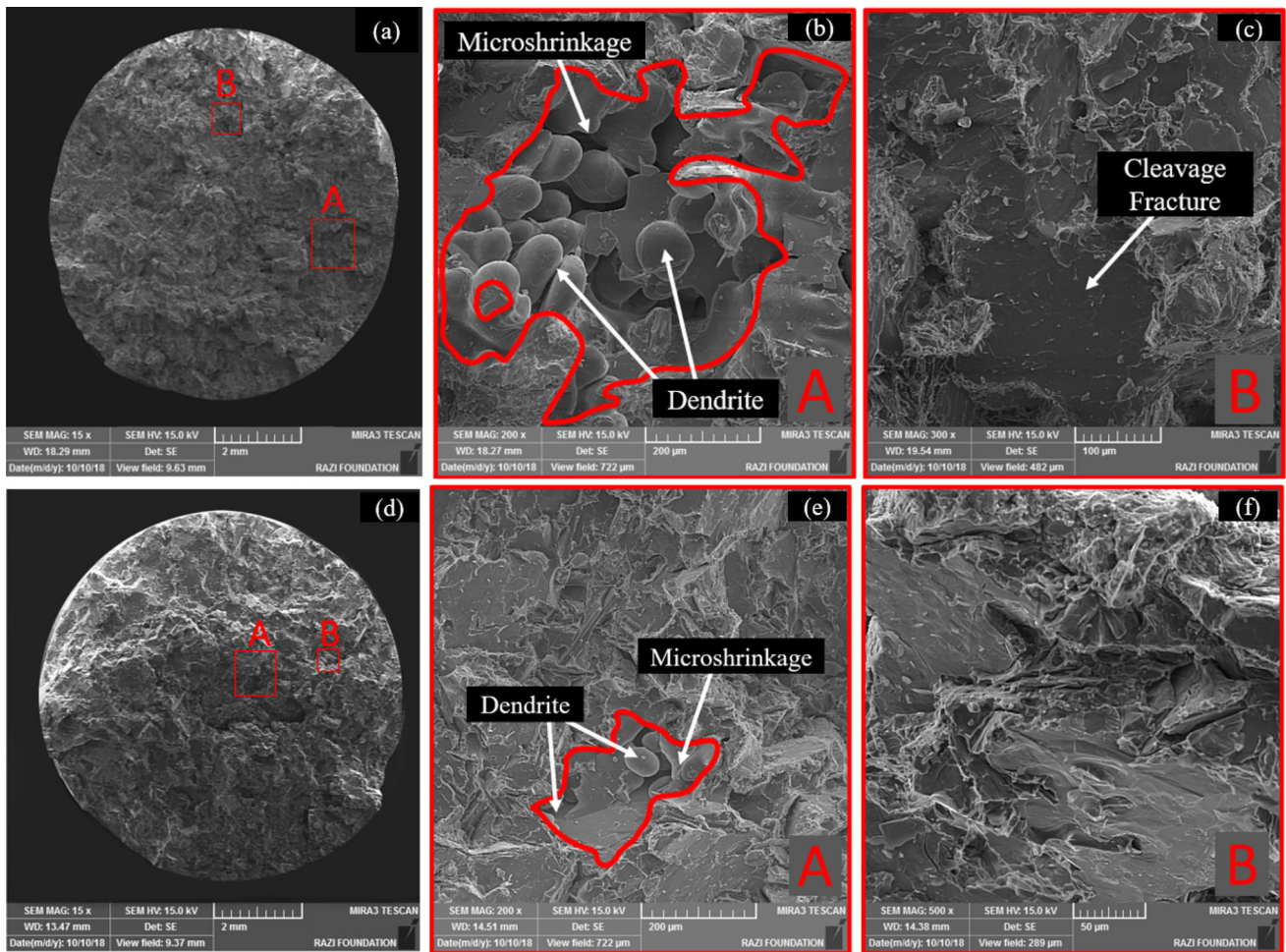


Figure 17. Fracture surfaces of the tensile test bars for (a, b, c) CSC-A413 and (d, e, f) DWS-A413.

The higher cooling rate during the DWS process can refine the DAS and SDAS so that the too small radius of the dendrite tip makes the interfacial energy of the fluid (S/L) interface higher than the grain boundary energy. Hence, the system prefers to replace the (S/L) interface with the grain boundaries, as evidenced in Figure 19. Therefore, the impinging dendrites coalesced and consequently formed an inter-connected network of dendrites throughout the casting. The increased ductility, yield strength, and ultimate tensile strength by the DWS process can be explained by this higher tendency of dendrites for coalescence due to their highly refined size [11, 15, 40–42].

That the response of A356 is better to the DWS process comparing to A413 is because of the lower liquid fraction at the time of coalescence. That is, in the A413 alloy, the liquid fraction is so high that the chance of impingement by growing dendrite is very low. In other words, there is always a layer of eutectic liquid between any two neighboring dendrite tips. In such conditions, a too refined dendritic structure cannot result in the creation of the

interconnected network; hence, no significant enhancement in the mechanical properties is achieved.

A summary of the effect of the DWS processing on the length of different microstructural features as compared to the CSC is shown in Figure 20. The DWS significantly decreases the SDAS, silicon blades size, brittle iron-bearing intermetallics, and divorced eutectic silicon size and thereby improves the tensile properties.

Conclusions

1. Applying the DWS increases the cooling rate from 0.05 to 0.19 °C/s in A413 and from 0.09 to 0.17 °C/s in A356 alloys. The solidification time was 83% shorter in DWS A413 and 67% in DWS A356 castings comparing to the corresponding counterparts.
2. In A356 samples, DWS can enhance the UTS from 126 to 193 MPa and elongation from 2.8 to 11%. The UTS of the DWS A413 was increased

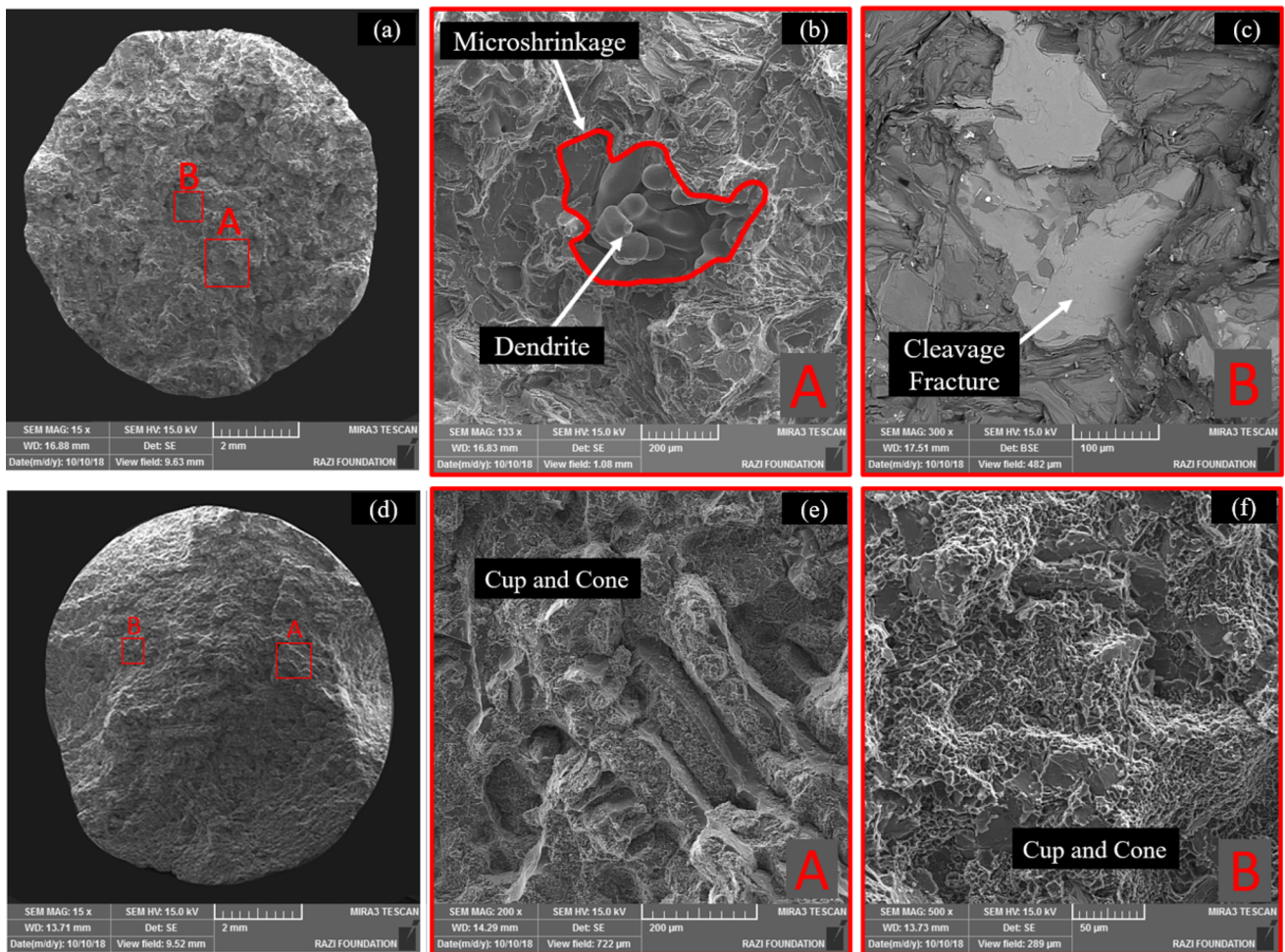


Figure 18. Fracture surfaces of the tensile test bars for (a, b, c) CSC-A356 and (d, e, f) DWS-A356.

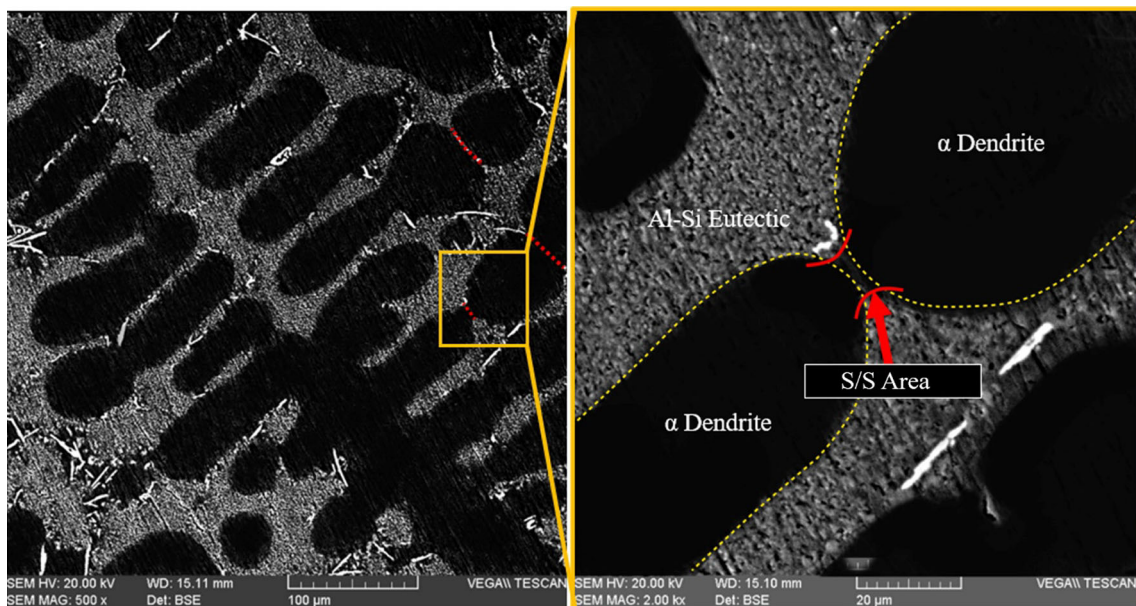


Figure 19. Microstructural evidences of the coalescence between dendrite arms of adjacent grains in the DWS-processed A356 alloy.

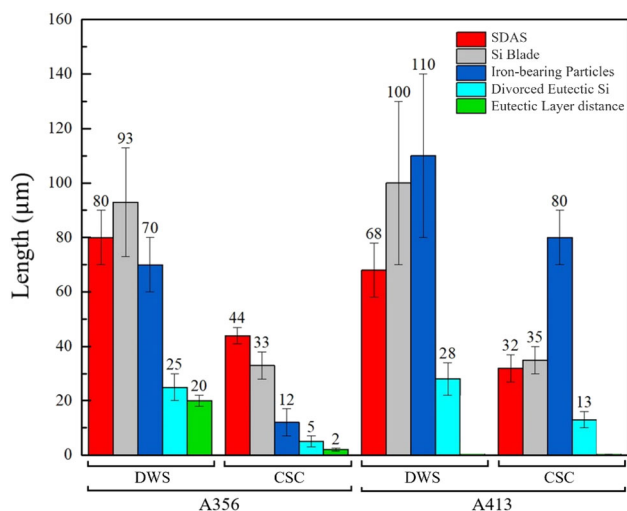


Figure 20. A summary of the effect of the DWS processing on the length of different microstructural features.

from 139 to 159 MPa while the elongation was improved from 1.8% to only 5%.

- The secondary dendrite arm spacing (SDAS) was decreased from 80 µm in A356 to 44 µm and from 68 µm in A413 to 32 µm in the respective DWS-processed counterparts.
- Despite providing the higher cooling rate by the DWS process comparing to the conventional sand casting, the results of tensile testing confirm that the enhancement in the tensile properties is significantly higher A356 comparing to A413. This can be attributed to the refinement of the primary phase as well as the lower liquid fraction at the final stages of solidification which help extensive coalescence and dendrite network formation by the primary phase in the A356 alloy. The higher liquid fraction between the refined dendrites of primary phase in the case of A413 alloy precludes the coalescence, and as a result, the enhancement in the tensile properties is not as significant as what achieved with the A356 alloy.

Conflict of interest On behalf of all authors, the corresponding author states that there is no conflict of interest.

REFERENCES

- J. Campbell: *Complete Casting Handbook: Metal Casting Processes, Techniques and Design*, 2nd edition. Amsterdam: Elsevier Butterworth-Heinemann, pp. 49–60 (2015).
- J. Campbell: *Castings Practice the 10 rules of casting*, 1st edition. Amsterdam: Elsevier Butterworth-Heinemann, pp 47–50 (2004).
- M. Vynnycky, Appl. Math. Model. **37**(4), 2178–2188 (2013)

- A. Zhang, S. Liang, Z. Guo, S. Xiong, Exp. Thermal Fluid Sci. **88**, 472–482 (2017)
- Z. Ma, A.M. Samuel, F.H. Samuel, H.W. Doty, S. Valtierra, Mater. Sci. Eng. A **490**(1–2), 36–51 (2008)
- J.A. Taylor, Proc. Mater. Sci. **1**, 19–33 (2012)
- X. Wu, H. Zhang, F. Zhang, Z. Ma, L. Jia, B. Yang, Bo, T. Tao, Mater. Charact. **139**, 116–124 (2018).
- S. Seifeddine, S. Johansson, I.L. Svensson, Mater. Sci. Eng. A **490**(1–2), 385–390 (2008)
- S.G. Shabestari, F. Shahri, J. Mater. Sci. **39**, 2023–2032 (2004)
- V.A. Hosseini, S.G. Shabestari, R. Gholizadeh, Mater. Des. **50**, 7–14 (2013)
- M. Pourgharibshahi, H. Saghafian, M. Divandari, F. Golestannejad, Int. J. Metalcast. **16**, 853–870 (2022)
- D. M. Stefanescu: *Science and Engineering of Casting Solidification*, 3d edition, Springer Cham, 2015.
- J. Grassi, J. Campbell, M. Hartlieb, J. Major, Ablation casting. In: *Aluminum alloys: fabrication, characterization, and applications*, eds. W. Yin & SK Das, (TMS, The Minerals, Metals, and Materials Society, 2008), 73-77 (2008).
- S.M.A. Boutorabi, P. Torkaman, J. Campbell et al., Structure and properties of carbon steel cast by the ablation process. Inter Metalcast **15**, 306–318 (2021). <https://doi.org/10.1007/s40962-020-00466-7>
- M. Salarvand, S.M.A. Boutorabi, M. Pourgharibshahi et al., Effect of cooling rate on the microstructure and mechanical properties of high-zinc AA 5182 aluminum wrought alloy cast by the ablation green sand mold casting process. Inter Metalcast **15**, 1464–1475 (2021). <https://doi.org/10.1007/s40962-021-00578-8>
- E. Barbarias, A. Niklas, I. Lizarralde, M. Garat, A. Bakedano, A.I. Fernández-Calvo, Mater. Sci. Eng. A **833**, 142528 (2022)
- E. Heidari, S.M.A. Boutorabi, M.T. Honaramooz et al., Ablation casting of thin-wall ductile iron. Inter Metalcast **16**, 166–177 (2022). <https://doi.org/10.1007/s40962-021-00579-7>
- M. Taghipourian, M. Mohammadaliha, S.M. Boutorabi, S.H. Mirdamadi, J. Mater. Process. Technol. **238**, 89–95 (2016)
- V. Bohlooli, M.S. Mahalli, S.M.A. Boutorabi, Acta Metal. Sinica (English Letters) **26**, 85–91 (2013)
- A. Kheirabi, M. Divandari, S.M.A. Boutorabi et al., Effect of the modified ablation casting process on the mechanical properties and microstructure of near Eutectic Al-Si alloy. Inter Metalcast **16**, 1557–1574 (2022). <https://doi.org/10.1007/s40962-021-00672-x>
- J. Grassi, J. Campbell, M. Hartlieb, F. Major, Mater. Sci. Forum **618–619**, 591–594 (2009)
- A. Baghani, A. Kheirabi, A. Bahmani, H. Khalilpour: Arch. Metall. Mater. **66**(2), 397–405 (2021).
- A. Baghani, A. Kheirabi, A. Bahmani, M. Tamizifar, P. Davami, M. Ostad Shabani, A. Mazahery, Proc. Inst. Mech. Eng. Part L J. Mater. Des. Appl. **232**(3), 230–241 (2018).

24. S. M. Miresmaeili, S. G. Shabestari, S. M. A. Boutorabi, *Int. J. Cast Metals Res.* 2003, **16**(6), 541–548 (2003).
25. E. Vandersluis, C. Ravindran, *Metallogr. Microstruct. Anal.* **6**, 89–94 (2017)
26. B. E. Sundquist, L. F. Mondolfo, *Trans. Metal. Soc. AIME.* **221**, 157–164 (1961).
27. M.M. Makhlof, H.V. Guthy, *J. Light Met.* **1**(4), 199–218 (2001)
28. R. Zhongming, J. Jinze, *J. Mater. Sci.* **27**, 4663–4666 (1992)
29. C.W. Onyia, B.A. Okorie, S.I. Neife, C.S. Obayi, *World J. Eng. Technol.* **1**(2), 9–16 (2013)
30. M. Pourgharibshahi, H. Saghafian, M. Divandari, G. Timelli, *Metal. Mater. Trans. A.* **50**, 326–335 (2019)
31. M. Pourgharibshahi, M. Divandari, H. Saghafian Larijani, P. Ashtari, *J. Mater. Process. Technol.* **250**, 203–219 (2017).
32. M. Pourgharibshahi, M. Divandari, H. Saghafian, G. Timelli, *Metall. Mater. Trans. A.* **51**, 4572–4583 (2020)
33. B. Cantor, *Phil. Trans. R. Soc. A* **2003**(361), 409–417 (1804)
34. K.T. Akhil, S. Arul, R. Sellamuthu, *Proc. Mater. Sci.* **5**, 362–368 (2014)
35. M. Tiryakioğlu, E. Tiryakioğlu, D.R. Askeland, *Int. J. Cast Met. Res.* **9**(5), 259–267 (1997)
36. M.O. Shabani, A. Mazahery, A. Bahmani, P. Davami, N. Varahram, *Kovove Mater* **49**(4), 253–258 (2011)
37. M. O. Shabani, A. Mazahery, *Arch. Metall. Mater.* **56**(3), 671–675 (2011).
38. Q.G. Wang, *Metall. and Mater. Trans. A.* **34**, 2887–2899 (2003)
39. Y. Nishida, W. Droste, S. Engler, *Metall. Trans. B* **17**, 833–844 (1986)
40. R.I. Mackay, J.E. Gruzleski, *Int. J. Cast Met. Res.* **10**(3), 131–145 (1997)
41. M. Rappaz, A. Jacot, W. J. Boettinger, *Metal. Mater. Trans. A.* **34**, 467–479.
42. V. Mathier, A. Jacot, M. Rappaz, *Modell. Simulat. Mater. Sci. Eng.* **12**(13), 497–490 (2004)

Publisher's Note Springer Nature remains neutral with regard to jurisdictional claims in published maps and institutional affiliations.

Springer Nature or its licensor (e.g. a society or other partner) holds exclusive rights to this article under a publishing agreement with the author(s) or other rightsholder(s); author self-archiving of the accepted manuscript version of this article is solely governed by the terms of such publishing agreement and applicable law.